



Thermal lattice Boltzmann simulations of natural convection with complex geometry

Kuen-Hau Lin, Chuan-Chieh Liao, Shao-Yu Lien, Chao-An Lin *

Department of Power Mechanical Engineering, National Tsing Hua University, Hsinchu 300, Taiwan

ARTICLE INFO

Article history:

Received 25 February 2012

Received in revised form 12 August 2012

Accepted 19 August 2012

Available online 5 September 2012

Keywords:

Thermal boundary conditions

Thermal lattice Boltzmann method

Complex geometry

Unsteady flow

Nature convection

ABSTRACT

Thermal boundary condition of lattice Boltzmann method to simulate natural convection embedded with complex solid object is proposed. This is achieved by denoting the closest nodes adjacent to the boundary in the fluid domain as boundary nodes of the flow domain. The temperature of the boundary node is obtained by linear interpolation between the temperature of the solid object and the second fluid node further away. Then distribution functions originates from the solid domain at the boundary nodes are modified using known distribution functions and correctors to satisfy the momentum and energy. The technique is examined by simulating thermal Couette flow with wall injection, transient thermal flow induced by an abruptly rotating heated ring and nature convection in an annulus between a square outer cavity and a circular inner cylinder. Numerical simulations indicate that this method is second order accurate, and all the numerical results are compatible with the benchmark solutions.

© 2012 Elsevier Ltd. All rights reserved.

1. Introduction

Numerical investigations of natural convection with embedded complex heating element in enclosure were widely explored due to their industrial applications. Traditionally this is performed using the Navier–Stokes approach [1–5]. On the other hand, Lattice Boltzmann method (LBM) [6–14] has been successfully applied to various hydrodynamic problems and the major advantage of the LBM is explicit formulation. However, its application to non-isothermal problem is limited because of the numerical instability for thermal models [15].

In general, the thermal lattice Boltzmann model (TLBM) can be categorized into multi-speed approach and the passive scalar model [16]. The major advantage of the passive scalar model over the multi-speed approach is the enhancement of the numerical stability and is thus commonly adopted. In the passive scalar thermal lattice Boltzmann models [16–18], a separate distribution function is used to solve for the temperature distribution. It should be noted that stability of the thermal model can be further enhanced by adopting the hybrid finite-difference approach [19,20].

On the other hand, because the lattice Boltzmann method adopts the Cartesian grid, thus difficulties encountered to model complex domain are twofolds. Firstly the representation of the complex geometry, since the Cartesian grid does not conform with the curved boundary [21–24]. Secondly the correct implementation of the boundary conditions, where incorrect distribution

functions originated from the solid nodes external to the flow domain are encountered during the streaming operation [25–28].

Various methodologies have been put forward to tackle the LBM simulation of complex geometry flows [21–24]. For example, Filippova and Hanel [21] proposed a method using a simple linear interpolation between a fictitious equilibrium distribution function and a well-chosen near-boundary distribution function. The weighting factor of the interpolation is determined by the distance between the boundary and the near-boundary lattice. Mei et al. [22] further improved its numerical stability. Lallemand and Luo [23] combined the bounce-back scheme and interpolation scheme to treat a moving curved boundary by the lattice Boltzmann method. The bounce-back scheme simulates a stationary boundary, and an additional term is added to implement a moving boundary. On the other hand, Chang et al. [24] adopted similar technique as in [29], where the fluid velocity of node adjacent to the solid boundary is obtained by linear interpolation between the Lagrangian marker and the second fluid node further away. Then distribution functions originates from the solid domain at the nodes adjacent to the solid curved boundary are modified using known distribution functions and correctors directly from the definitions of density and momentum. Alternatively, the immersed boundary method (IBM) is another convenient approach to treat fluid flows involving complex boundary [30].

However, thermal LBM simulations with complex geometry are not common. In the present study, the previously proposed technique [24] to model complex geometry flows is extended to model the thermal flow with embedded complex solid object. Here, the curved boundary is represented by a series of Lagrangian markers.

* Corresponding author.

E-mail address: calin@pme.nthu.edu.tw (C.-A. Lin).

Nomenclature

c	lattice speed
C_s	speed of sound
D	diameter
dt	time step
dx	lattice width
\vec{e}_i	particle speed direction
f_i	particle density distribution function
\vec{g}	gravitational acceleration
g_i	particle energy distribution function
G	buoyancy term
G_c	correction to enforce the internal energy
H	channel height
$J_0(x)$	Bessel function of the first kind of order 0
$J_1(x)$	Bessel function of the first kind of order 1
k	thermal conductivity
L	height of the cavity
n	normal direction to the wall
Nu	local Nusselt number
\bar{Nu}	surface-averaged Nusselt number
Pr	Prandtl number = ν/α
Q	correction to enforce the required momentum
R	radius
Ra	Rayleigh number = $g\beta\Delta TL^3/\alpha\nu$
Re	Reynolds number
S	half of the perimeter of circular cylinder
t	time

T	temperature
ΔT	temperature difference
\vec{u}	velocity vector
V_0	injection velocity
\vec{x}	position vector

Greek symbols

α	thermal diffusivity
α_n^0	n th zero roots of $J_0(x)$
α_n^1	n th zero roots of $J_1(x)$
β	thermal expansion coefficient
ϵ	distance between the cavity and cylinder center
θ	angle from the top of circular cylinder
ρ	macroscopic density
τ_f	relaxation time for velocity field
τ_g	relaxation time for thermal field
ν	kinematic viscosity
ϕ	angle between lines \overrightarrow{AB} and \overrightarrow{BC} in Fig. 8
χ	thermal diffusivity
ω_i	weighting factor in the LBM

Superscripts and subscripts

eq	equilibrium
$+$	post collision
$*$	local known value
i	lattice link number

The temperature of node adjacent to the solid boundary is obtained by linear interpolation between the Lagrangian marker and the second fluid node further away. Then distribution functions originates from the solid domain at the nodes adjacent to the solid curved boundary are modified using known distribution functions and correctors, where the correctors at these nodes are obtained directly from the definition of temperature. The validity and the accuracy of the new method are scrutinized by simulating thermal Couette flow with wall injection, transient thermal induced by an abruptly rotating ring and nature convection within a square cavity embedded complex solid object.

2. The thermal lattice Boltzmann method

The thermal lattice Boltzmann equation adopting a uniform lattice with Bhatnagar–Gross–Krook collision model [6,31] can be expressed as

$$f_i^+(\vec{x}, t) = f_i(\vec{x}, t) - \frac{1}{\tau_f} [f_i(\vec{x}, t) - f_i^{eq}(\vec{x}, t)] \quad (1)$$

$$f_i(\vec{x} + \vec{e}_i dt, t + dt) = f_i^+(\vec{x}, t) \quad (2)$$

$$g_i^+(\vec{x}, t) = g_i(\vec{x}, t) - \frac{1}{\tau_g} [g_i(\vec{x}, t) - g_i^{eq}(\vec{x}, t)] \quad (3)$$

$$g_i(\vec{x} + \vec{e}_i dt, t + dt) = g_i^+(\vec{x}, t) \quad (4)$$

where f_i and g_i are the particle density and energy distribution functions along the particle velocity direction \vec{e}_i , respectively, f_i^{eq} and g_i^{eq} are the equilibrium distribution functions, and τ_f and τ_g are the dimensionless relaxation times that control the rates approaching equilibrium.

Based on the distribution functions, the macroscopic density ρ , velocity \vec{u} and temperature T are defined as

$$\sum_i f_i = \rho, \quad \sum_i f_i \vec{e}_i = \rho \vec{u}, \quad \sum_i g_i = \rho T \quad (5)$$

The equilibrium distribution functions, which depend on the local density and velocity, are given by the form [6,31]

$$f_i^{eq} = \omega_i \rho \left[1 + \frac{3\vec{e}_i \cdot \vec{u}}{c^2} + \frac{9(\vec{e}_i \cdot \vec{u})^2}{2c^4} - \frac{3\vec{u} \cdot \vec{u}}{2c^2} \right] \quad (6)$$

$$g_i^{eq} = \omega_i \rho T \left[1 + \frac{3\vec{e}_i \cdot \vec{u}}{c^2} + \frac{9(\vec{e}_i \cdot \vec{u})^2}{2c^4} - \frac{3\vec{u} \cdot \vec{u}}{2c^2} \right] \quad (7)$$

$c = dx/dt$ is the lattice speed, where dx and dt are the lattice width and time step, respectively. Here, dt is chosen to be equal to dx , thus $c = 1$. ω_i is a weighting factor. For the present 2D applications, D2Q9 model are adopted. The particle speed \vec{e}_i adopting D2Q9 model are defined as

$$\vec{e}_0 = 0 \quad (8)$$

$$\vec{e}_i = (\cos[\pi(i-1)/2], \sin[\pi(i-1)/2])c \quad i = 1, 2, 3, 4 \quad (9)$$

$$\vec{e}_i = (\cos[\pi(i-4-1/2)/2], \sin[\pi(i-4-1/2)/2])\sqrt{2}c \quad i = 5, 6, 7, 8 \quad (10)$$

where the weighting factors ω_i are $\omega_0 = 4/9$, $\omega_{i=1\sim 4} = 1/9$, $\omega_{i=5\sim 8} = 1/36$ for D2Q9 model. The corresponding kinematic viscosity and thermal diffusivity are calculated by $\nu = (\tau_f - 0.5)C_s^2 dt$ and $\chi = (\tau_g - 0.5)C_s^2 dt$, where $C_s = c/\sqrt{3}$ is the speed of sound.

3. Boundary conditions

A typical computational domain with a solid object embedded within is shown in Fig. 1. In the present approach, LBM simulation is applied throughout the computational domain, i.e. even within the solid. Therefore, two different boundary conditions have to be addressed. The first one is the boundary condition along the computational domain (thick solid line), and the second one is how to represent the solid–fluid boundary. Here, the derivation of the boundary condition is based on the known or assumed

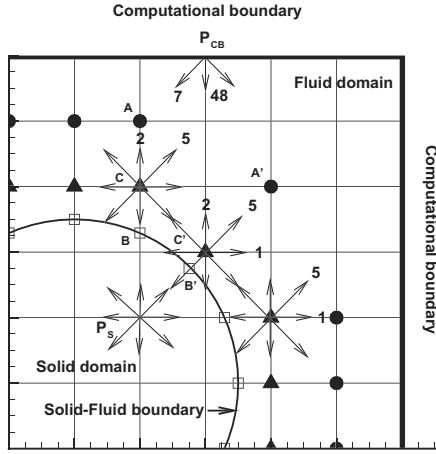


Fig. 1. Distribution functions along the boundary nodes. ▲: correction node, □: Lagrangian marker, ●: second fluid node.

velocity and temperature (u, v, T) distributions along these boundaries.

3.1. Computational domain

3.1.1. Hydrodynamic boundary conditions

Before proceeding to the discussions of the boundary conditions of the lattice Boltzmann methods, it is beneficial here to derive first the discrete form of the macroscopic momentum equation based on the lattice Boltzmann equations, i.e. Eqs. (1)–(4), (6) and (7). Since general discrete forms are difficult to derive, the focus here is concentrated on the D2Q9 steady fully developed channel flow driven by a fixed body force (G) with periodic boundary conditions. The discrete Navier–Stokes equation for steady fully developed channel flow has been derived by [27,32] and is expressed as

$$\frac{u_{j+1} v_{j+1} - u_{j-1} v_{j-1}}{2dx} = \underbrace{\frac{2\tau_f - 1}{6} \frac{dx^2}{dt}}_v \frac{u_{j-1} - 2u_j + u_{j+1}}{dx^2} + G + \frac{\tau_f - 1}{dt} [\mathbf{u}_{j-1} - u_{j-1} + \mathbf{u}_{j+1} - u_{j+1}] - \frac{2\tau_f^2 - 2\tau_f + 1}{\tau_f dt} [\mathbf{u}_j - u_j] \quad (11)$$

where u and v are streamwise and transverse velocity, respectively and j is the discrete index in the transverse direction. It should be noted, however, that \mathbf{u} and u are defined in Eqs. (5) and (6), respectively. Except in the boundary, $\mathbf{u} = u$. Thus the equation reduces to the second order accurate central difference equation. For steady fully developed channel flow without transverse wall injection ($v = 0$), the equation predicts exact parabolic profiles.

The influence of the boundary condition can be verified by considering the discrete form of the macroscopic momentum equation next to the lower wall, i.e.

$$\frac{u_3 v_3 - u_1 v_1}{2dx} = \underbrace{\frac{2\tau_f - 1}{6} \frac{dx^2}{dt}}_v \frac{u_1 - 2u_2 + u_3}{dx^2} + G + \frac{\tau_f - 1}{dt} [\mathbf{u}_1 - u_1] \quad (12)$$

where index $j = 1$ locates the lower wall. u_1 is no slip wall velocity and \mathbf{u}_1 is computed by the wall distribution function, i.e. $\rho \mathbf{u}_1 = C(f_1^{j=1} + f_5^{j=1} + f_8^{j=1} - f_3^{j=1} - f_6^{j=1} - f_7^{j=1})$. It is clear that $f_2^{j=1}$, $f_3^{j=1}$, and $f_6^{j=1}$ are to be determined at the wall. He et al. [32] concluded that, slip velocity is zero as long as $\mathbf{u}_1 = u_1$ regardless of the formulation

of $f_2^{j=1}$, $f_3^{j=1}$, and $f_6^{j=1}$. This provides a guide to determine the unknown density population.

Boundary condition proposed in [24,27] is employed to determine the unknown particle density distribution functions along the boundary, which are expressed as a combination of the local known value and a corrector

$$f_p(\vec{x}, \vec{e}_p, t) = f_p^*(\vec{x}, \vec{e}_p, t) + \frac{\omega_p}{c} \vec{e}_p \cdot \vec{Q} \quad (13)$$

where \vec{Q} is the corrector to enforce the required momentum. For instance, consider a node (P_{CB}) at the top boundary as shown in Fig. 1, where the unknown density distribution functions are f_4 , f_7 , and f_8 , i.e. $f_4 = f_4^* - \omega_4 Q_y$, $f_7 = f_7^* - \omega_7 (Q_x + Q_y)$, and $f_8 = f_8^* + \omega_8 (Q_x - Q_y)$. Therefore, the macroscopic velocity and density at the node using Eq. (5) in conjunction with Eq. (13), can be expressed as

$$\rho = f_0 + f_1 + f_2 + f_3 + (f_4^* - \omega_4 Q_y) + f_5 + f_6 + [f_7^* - \omega_7 (Q_x + Q_y)] + [f_8^* + \omega_8 (Q_x - Q_y)] \quad (14)$$

$$\rho u = f_1 + f_5 + [f_8^* + \omega_8 (Q_x - Q_y)] - f_3 - f_6 - [f_7^* - \omega_7 (Q_x + Q_y)] \quad (15)$$

$$\rho v = f_2 + f_5 + f_6 - (f_4^* - \omega_4 Q_y) - [f_7^* - \omega_7 (Q_x + Q_y)] - [f_8^* + \omega_8 (Q_x - Q_y)] \quad (16)$$

If velocities u and v are known at the boundary, Eqs. (14)–(16) can be used to solve for ρ , Q_x , and Q_y , and then f_4 , f_7 , and f_8 are obtained. For simplicity, $f_p^*(\vec{x}, \vec{e}_p, t) = f_p(\vec{x}, -\vec{e}_p, t)$ are adopted. It should be noted that the influence of the choice of the local known distribution function f^* is negligible [27]. The explicit forms of the unknown particle density distribution functions are shown as below:

$$\rho = \frac{1}{1+v} [f_0 + f_1 + f_3 + 2(f_2 + f_5 + f_6)] \quad (17)$$

$$f_4 = f_2 - \frac{2}{3} \rho v \quad (18)$$

$$f_7 = f_5 + \frac{1}{2} (f_1 - f_3) - \frac{1}{2} \rho u - \frac{1}{6} \rho v \quad (19)$$

$$f_8 = f_6 - \frac{1}{2} (f_1 - f_3) + \frac{1}{2} \rho u - \frac{1}{6} \rho v \quad (20)$$

3.1.2. Thermal boundary conditions

Using similar technique, the discrete temperature equation can be derived for fully developed channel flow [18]. Here, for simplicity, the body force is neglected. Using Eqs. (3), (4) and (7), the result is

$$\frac{T_{j+1} v_{j+1} - T_{j-1} v_{j-1}}{2dx} = \underbrace{\frac{2\tau_g - 1}{6} \frac{dx^2}{dt}}_x \frac{T_{j-1} - 2T_j + T_{j+1}}{dx^2} + \frac{\tau_g - 1}{dt} \times [\mathbf{T}_{j-1} - T_{j-1} + \mathbf{T}_{j+1} - T_{j+1}] - \frac{2\tau_g^2 - 2\tau_g + 1}{\tau_g dt} [\mathbf{T}_j - T_j] \quad (21)$$

Again, if the temperature \mathbf{T} defined by the distribution function Eq. (5) is the same as that T used in the equilibrium distribution function Eq. (7), then the equation reduces to the second order accurate central difference equation.

The influence of the thermal boundary condition can be verified by considering the above equation next to the lower wall, i.e.

$$\frac{T_3 v_3 - T_1 v_1}{2dx} = \underbrace{\frac{2\tau_g - 1}{6} \frac{dx^2}{dt}}_x \frac{T_1 - T_2 + T_3}{dx^2} + \frac{\tau_g - 1}{dt} [\mathbf{T}_1 - T_1] \quad (22)$$

where T_1 is the wall temperature and \mathbf{T}_1 is determined by the energy distribution function, i.e. $\rho \mathbf{T}_1 = g_0^{j=1} + g_1^{j=1} + g_2^{j=1} + g_3^{j=1} +$

$g_4^{j=1} + g_5^{j=1} + g_6^{j=1} + g_7^{j=1} + g_8^{j=1}$. It is clear that $g_2^{j=1}$, $g_5^{j=1}$, $g_6^{j=1}$ are to be determined at the wall. Similar to the momentum equation, the above equation produces correct answer as long as $T_1 = T_1$. This provides a guide to determine the unknown energy distribution population at the wall.

Here, similar to its hydrodynamic counterpart, a consistent thermal boundary condition is introduced [18]. The unknown particle energy distribution function at the plane boundary is assumed to be

$$g_p(\vec{x}, \vec{e}_p, t) = g_p^*(\vec{x}, \vec{e}_p, t) + \omega_p G_c \quad (23)$$

where G_c is the correction to enforce the internal energy. The influence of different local known distribution functions g^* is found to be negligible [18], and $g_p^*(\vec{x}, \vec{e}_p, t) = g_p^{eq}(\vec{x}, \vec{e}_p, t)$ is adopted here.

For instance, consider a node (P_{CB}) at the top boundary as shown in Fig. 1, where the unknown particle energy distribution functions are (g_4, g_7, g_8). Therefore, the internal energy density at the node using Eq. (5), in conjunction with Eq. (23), can be expressed as

$$\rho T = g_0 + g_1 + g_2 + g_3 + [g_4^* + \omega_4 G_c] + g_5 + g_6 + [g_7^* + \omega_7 G_c] + [g_8^* + \omega_8 G_c] \quad (24)$$

$$\rho T^* = g_0 + g_1 + g_2 + g_3 + g_4^* + g_5 + g_6 + g_7^* + g_8^* \quad (25)$$

$$G_c = \frac{\rho T - \rho T^*}{\omega_4 + \omega_7 + \omega_8} \quad (26)$$

The temperature T is known at the boundary, hence (g_4, g_7, g_8) are obtained for D2Q9 model. The explicit forms of the unknown particle energy distribution functions are shown as below.

$$T^* = \frac{1}{\rho} (g_0 + g_1 + g_2 + g_3 + g_4^* + g_5 + g_6 + g_7^* + g_8^*) \quad (27)$$

$$g_4 = g_4^* + \frac{2}{3} \rho (T - T^*) \quad (28)$$

$$g_7 = g_7^* + \frac{1}{6} \rho (T - T^*) \quad (29)$$

$$g_8 = g_8^* + \frac{1}{6} \rho (T - T^*) \quad (30)$$

3.2. The solid–fluid boundary technique

Here, technique employed in [24] to model the solid–fluid boundary is introduced, since the boundary does not in general coincides with the lattices. A typical solid–fluid boundary within the computational domain is shown in Fig. 1, where the closest nodes adjacent to the boundary in the fluid domain are termed the correction nodes (C) as represented by the filled triangles. The open squares are the Lagrangian markers (B) used to mimic the solid–fluid boundary, and the filled circles represent the second fluid nodes (A) beyond the correction nodes. In the present curved boundary approach, the correction nodes are used to impose the momentum and energy conditions due to the presence of the solid–fluid boundary.

The correct macroscopic quantities of the correction nodes are obtained by linear interpolation between the velocities and temperature of the Lagrangian marker (B) and the second fluid node (A), as shown in Fig. 2.

$$\phi_C = \vec{V}_A - (\phi_A - \phi_B) \frac{\overline{AC}}{\overline{AB}} \quad (31)$$

The determination of the location of the Lagrangian marker is addressed here. If the correction node one vertical or horizontal edge connected with the solid–fluid boundary, for example at node C, the Lagrangian marker is determined as the intersection of the line \overline{AC} with the solid–fluid boundary, i.e. marker point B. How-

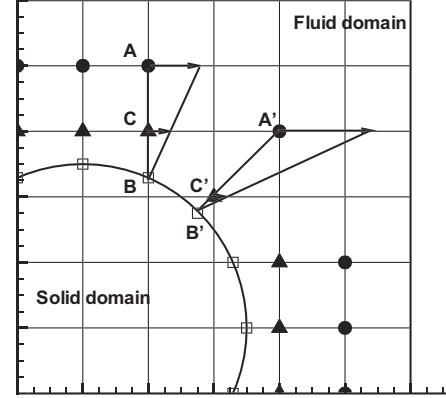


Fig. 2. Geometry of flows with an immersed boundary. \blacktriangle : correction node, \square : Lagrangian marker, \bullet : second fluid node.

ever, for node C' there are one vertical and one horizontal edges connected to the solid–fluid boundary. Therefore, the interpolation is not unique. In order to avoid this ambiguity, the method proposed in [4,29] (using the Navier–Stokes solver) is adopted, that the Lagrangian marker is determined as the intersection of the line $\overline{A'C'}$ with the solid–fluid boundary, i.e. marker point B' .

As indicated earlier, LBM simulation is applied throughout the computational domain even within the solid domain, i.e. at point P_s . Therefore, after the streaming operation, distribution functions originated from the solid domain, $f_p^+(\vec{x} - \vec{e}_i dt, t - dt)$ and $g_p^+(\vec{x} - \vec{e}_i dt, t - dt)$, will migrate to the correction nodes adjacent to the solid–fluid boundary, for example nodes C: f_2, f_5, g_2, g_5 and C' : $f_1, f_2, f_5, g_1, g_2, g_5$ shown in Fig. 1. Obviously, the momentum and energy based on these distribution functions will not be correct. Thus, measures have to be taken to modify these incorrect particle distribution functions to satisfy the momentum and energy condition (u_c, v_c, T_c) computed by Eq. (31).

Therefore, the particle distribution functions at these nodes are modified as

$$f_p(\vec{x}, t) = f_p^+(\vec{x} - \vec{e}_i dt, t - dt) + \frac{\omega_p}{c} \vec{e}_p \cdot \vec{Q} \quad (32)$$

$$g_p(\vec{x}, t) = g_p^+(\vec{x} - \vec{e}_i dt, t - dt) + \frac{\omega_p}{c} G_c \quad (33)$$

Consider, for example correction node C' shown in Fig. 1, where the distribution functions needed for modification are

$$f_1 = f_1^+(\vec{x} - \vec{e}_1 dt, t - dt) + \omega_1 Q_x \quad (34)$$

$$f_2 = f_2^+(\vec{x} - \vec{e}_2 dt, t - dt) + \omega_2 Q_y \quad (35)$$

$$f_5 = f_5^+(\vec{x} - \vec{e}_5 dt, t - dt) + \omega_5 (Q_x + Q_y) \quad (36)$$

$$g_1 = g_1^+(\vec{x} - \vec{e}_1 dt, t - dt) + \omega_1 G_c \quad (37)$$

$$g_2 = g_2^+(\vec{x} - \vec{e}_2 dt, t - dt) + \omega_2 G_c \quad (38)$$

$$g_5 = g_5^+(\vec{x} - \vec{e}_5 dt, t - dt) + \omega_5 G_c \quad (39)$$

Therefore, the macroscopic quantities at the point C' using Eqs. (5) and (34)–(39) can be expressed as

$$\begin{aligned} \rho &= f_0 + f_1^+(\vec{x} - \vec{e}_1 dt, t - dt) + \omega_1 Q_x + f_2^+(\vec{x} - \vec{e}_2 dt, t - dt) \\ &\quad + \omega_2 Q_y + f_3 + f_4 + f_5^+(\vec{x} - \vec{e}_5 dt, t - dt) + \omega_5 (Q_x + Q_y) \\ &\quad + f_6 + f_7 + f_8 \end{aligned} \quad (40)$$

$$\begin{aligned} \rho u_c &= f_1^+(\vec{x} - \vec{e}_1 dt, t - dt) + \omega_1 Q_x + f_5^+(\vec{x} - \vec{e}_5 dt, t - dt) \\ &\quad + \omega_5 (Q_x + Q_y) + f_8 - f_3 - f_6 - f_7 \end{aligned} \quad (41)$$

$$\begin{aligned} \rho v_c &= f_2^+(\vec{x} - \vec{e}_2 dt, t - dt) + \omega_2 Q_y + f_5^+(\vec{x} - \vec{e}_5 dt, t - dt) \\ &\quad + \omega_5 (Q_x + Q_y) + f_6 - f_4 - f_7 - f_8 \end{aligned} \quad (42)$$

$$\begin{aligned} \rho T_C = & g_0 + g_1^+(\vec{x} - \vec{e}_1 dt, t - dt) + \omega_1 G_C + g_2^+(\vec{x} - \vec{e}_2 dt, t - dt) \\ & + \omega_2 G_C + g_3 + g_4 + g_5^+(\vec{x} - \vec{e}_5 dt, t - dt) + \omega_5 G_C + g_6 \\ & + g_7 + g_8 \end{aligned} \quad (43)$$

It should be noted that unlike the flat boundary, the number and the direction of the incorrect distribution functions at each correction node are different along the curved boundary. Therefore, no explicit solution of (40)–(43) is derived here. For temperature, the computation of G_C is straightforward, and thus g_1 , g_2 and g_5 can be obtained. On the other hand, matrix inversion is used to obtain density and correctors (Q_x , Q_y), and hence f_1 , f_2 and f_5 . It is noted that the matrix coefficients are functions of the weighting functions of the incorrect distribution functions and are independent of the distance of the correction nodes to the wall. Similar procedure can be applied to other correction nodes to enforce the correct momentum.

4. Numerical results

4.1. Thermal Couette flow with wall injection

Attention is directed first to the two-dimensional thermal Couette flow with wall injection. This is to examine the validity of the proposed thermal LBM and boundary conditions at moving wall. Here, the channel top wall is moving at a constant velocity U_t with a higher constant temperature T_t , and the bottom wall is stationary with a lower constant temperature T_b . Fluid is injected from the bottom wall into the channel and extracted from the top moving wall with a vertical component V_0 . The major control parameters are the Prandtl number and the Reynolds number defined based on the injection velocity V_0 and channel height H , i.e. $Re = V_0 H / \nu$. The analytic solution for this temperature field is shown below:

$$T_{exact}(y) = T_b + \left(\frac{e^{PrRe} y/H - 1}{e^{PrRe} - 1} \right) \Delta T \quad (44)$$

Velocity boundary conditions and the proposed Dirichlet thermal boundary conditions are applied along the channel walls, and periodic boundary conditions are applied at the inlet and outlet. Fig. 3 shows the temperature profiles in comparison with the analytic solution for different Reynolds numbers while the Prandtl number is fixed. Five different lattice densities in the y direction are adopted (21, 41, 81, 161, and 321), to determine the convergence rate in space. Fig. 4 shows the predicted results and the second-order accuracy is achieved.

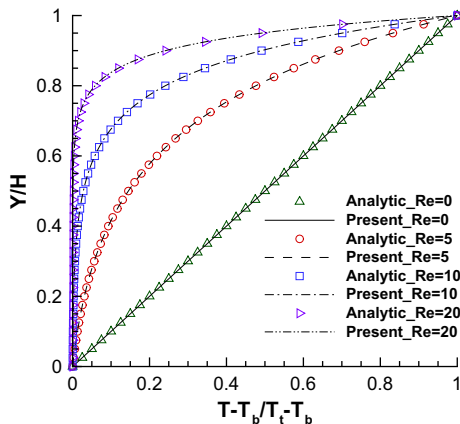


Fig. 3. The temperature profiles of 2-D Couette flow with wall injection when $Pr = 0.71$.

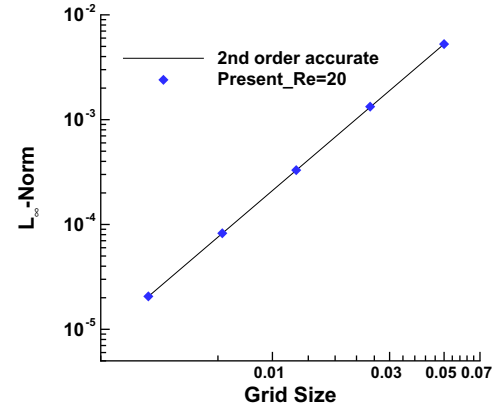


Fig. 4. Maximum predicted temperature errors of 2-D Couette flow with wall injection.

4.2. Transient flow induced by an abruptly rotating ring

Here, the flow considered is a ring rotating at the center of a square domain $[-D, D] \times [-D, D]$, where $D (= 2R)$ the diameter of the rotating ring is 1. The dimensionless relaxation times are $\tau_f = 0.65$ and $\tau_g = 0.71$. The corresponding Reynolds and Prandtl numbers are $U_{0max} D / \nu = 10$ and $Pr = 0.71$. Numerical mesh adopted is 160×160 . Since the ring starts abruptly from rest, the flow inside the ring is driven by the rotating ring. After the transient stage, the flow reaches solid body rotation state within the ring. The initial temperature distribution inside the ring is set as zero with a T_{cyl} ring temperature. The analytic solution for this rotating ring can be expressed as

$$u_\theta = \sum_{n=1}^{\infty} A_n \exp\left(-\frac{\nu(\alpha_n^1)^2 t}{R^2}\right) J_1\left(\frac{\alpha_n^1 r}{R}\right) + r\Omega \quad (45)$$

$$T = \sum_{n=1}^{\infty} B_n \exp\left(-\frac{\chi(\alpha_n^0)^2 t}{R^2}\right) J_0\left(\frac{\alpha_n^0 r}{R}\right) + T_B \quad (46)$$

where

$$A_n = \frac{\int_0^R -r^2 \Omega J_1\left(\frac{\alpha_n^1 r}{R}\right) dr}{\int_0^R r J_1^2\left(\frac{\alpha_n^1 r}{R}\right) dr} \quad (47)$$

$$B_n = \frac{\int_0^R -r T_{cyl} J_0\left(\frac{\alpha_n^0 r}{R}\right) dr}{\int_0^R r J_0^2\left(\frac{\alpha_n^0 r}{R}\right) dr} \quad (48)$$

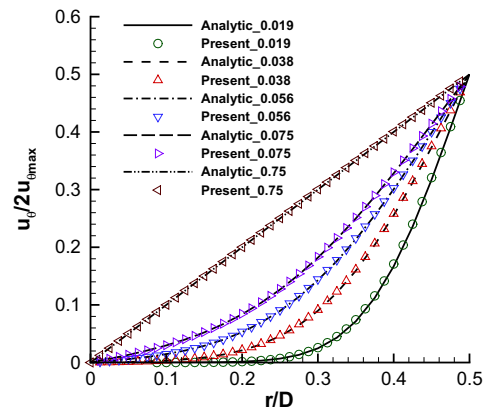


Fig. 5. Transient variations of velocity compared with analytic resolution.

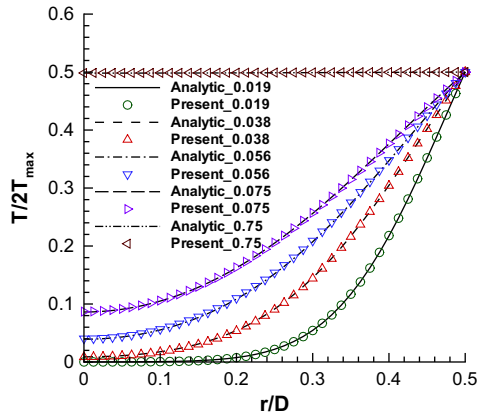


Fig. 6. Transient variations of temperature compared with analytic resolution.

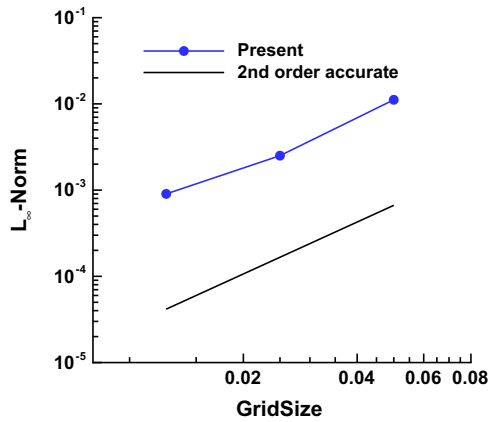


Fig. 7. Maximum predicted temperature error of rotating ring.

Table 1

Comparison of predicted surface-averaged Nusselt number (\overline{Nu}) with Shu et al. [35] and Moukalled and Acharya [2] for simulating 2-D natural convection of concentric cylinder in a square cavity.

L/D	Ra	Present	Shu et al. [35]	Moukalled and Acharya [2]
5.0	10^4	2.081	2.082	2.071
2.5	10^4	3.229	3.245	3.331
1.67	10^4	5.183	5.395	5.826
5.0	10^5	3.801	3.786	3.825
2.5	10^5	4.924	4.861	5.080
1.67	10^5	6.147	6.214	6.212
5.0	10^6	6.108	6.106	6.107
2.5	10^6	9.680	8.898	9.374
1.67	10^6	11.954	12.000	11.620

Table 2

The predicted \overline{Nu} for simulating 2-D natural convection of the eccentric cylinder ($\epsilon = 0.25 L$) at different location angles (ϕ) in a square cavity when $Ra = 3 \times 10^5$.

ϕ	0°	45°	90°	135°	180°
Present	7.98	6.85	7.43	6.04	6.97

$$J_0(x) = \sum_{m=0}^{\infty} \frac{(-1)^m}{(m!)^2} \left(\frac{x}{2}\right)^{2m} \quad (49)$$

$$J_1(x) = \sum_{m=0}^{\infty} \frac{(-1)^m}{m! \Gamma(m+2)} \left(\frac{x}{2}\right)^{2m+1} \quad (50)$$

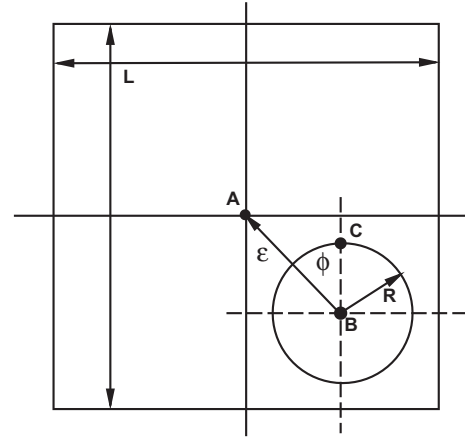


Fig. 8. Geometry of nature convection of a heated inner cylinder within a square cavity.

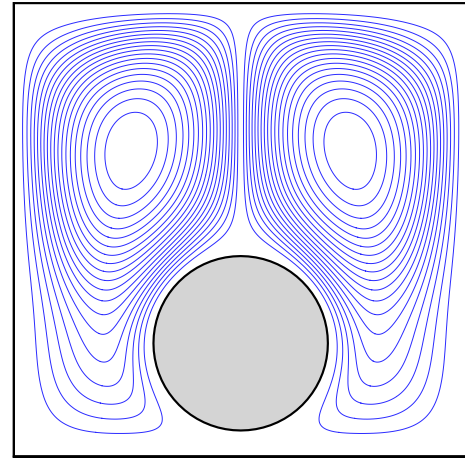


Fig. 9. Predicted streamlines at $\phi = 0^\circ$, $Ra = 3 \times 10^5$, and $L/D = 2.6$.

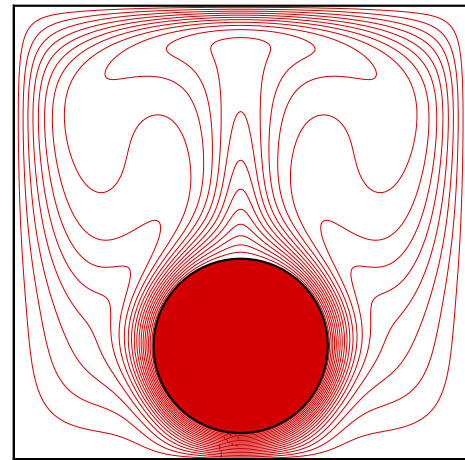


Fig. 10. Predicted isotherms at $\phi = 0^\circ$, $Ra = 3 \times 10^5$, and $L/D = 2.6$.

and α_n^0 and α_n^1 are the n th zero roots of $J_0(x)$ and $J_1(x)$, respectively.

Numerical solutions are compared with the analytic solutions as shown in Figs. 5 and 6 at different time $t^* = vt/R^2$. The migration of the flow from rest to solid body rotation profiles can be clearly observed. Also, the transient developments of the temperature also

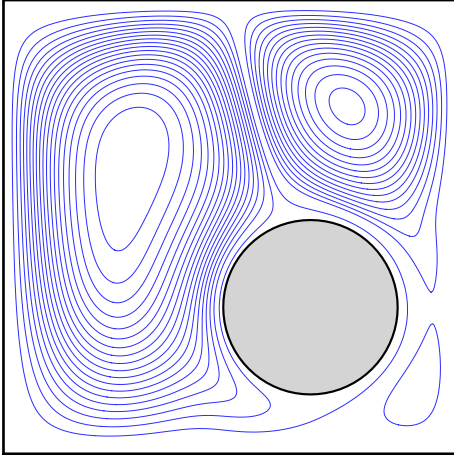


Fig. 11. Predicted streamlines at $\phi = 45^\circ$, $Ra = 3 \times 10^5$, and $L/D = 2.6$.

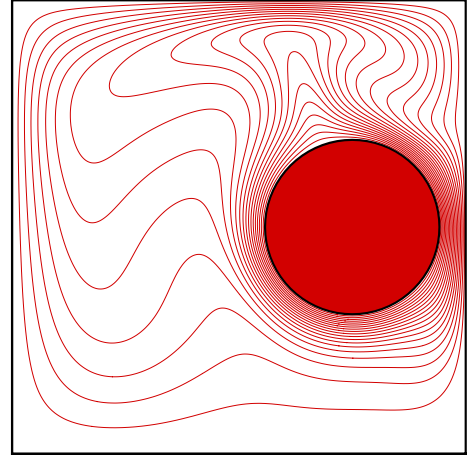


Fig. 14. Predicted isotherms at $\phi = 90^\circ$, $Ra = 3 \times 10^5$, and $L/D = 2.6$.

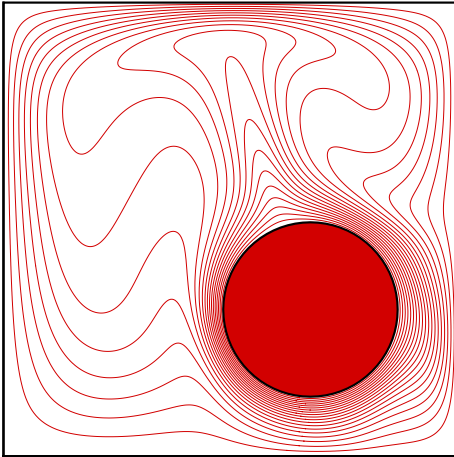


Fig. 12. Predicted isotherms at $\phi = 45^\circ$, $Ra = 3 \times 10^5$, and $L/D = 2.6$.

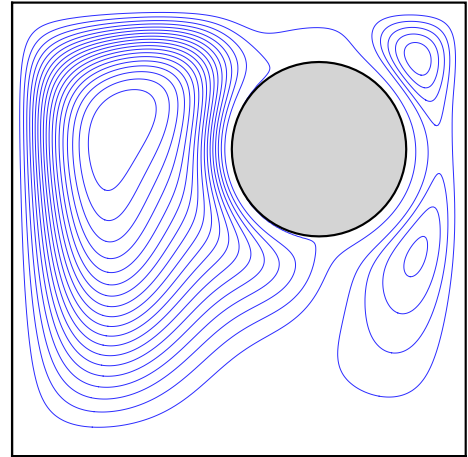


Fig. 15. Predicted streamlines at $\phi = 135^\circ$, $Ra = 3 \times 10^5$, and $L/D = 2.6$.

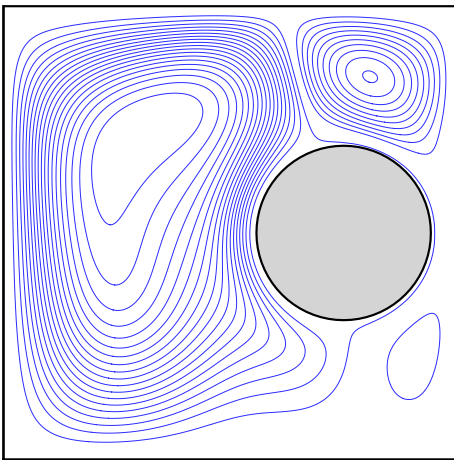


Fig. 13. Predicted streamlines at $\phi = 90^\circ$, $Ra = 3 \times 10^5$, and $L/D = 2.6$.

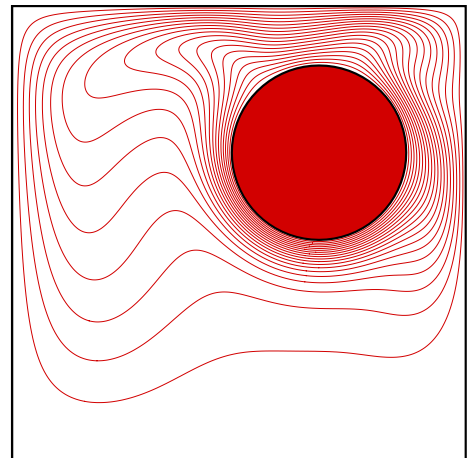


Fig. 16. Predicted isotherms at $\phi = 135^\circ$, $Ra = 3 \times 10^5$, and $L/D = 2.6$.

indicate a tendency towards a uniform temperature distribution. Numerical solutions agree well with the analytic solutions, indicating the accuracy of the present methodology. The maximum error norm is shown in Fig. 7, which also indicates the accuracy of the present scheme.

4.3. Natural convection in an annulus between a square cavity and a circular inner cylinder

In the present section, the natural convection in an annulus between a square cavity and a circular inner cylinder is investigated, where the flow is bounded by a stationary square enclosure with

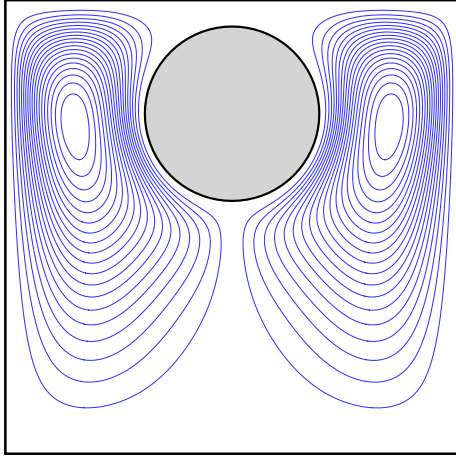


Fig. 17. Predicted streamlines at $\phi = 180^\circ$, $Ra = 3 \times 10^5$, and $L/D = 2.6$.

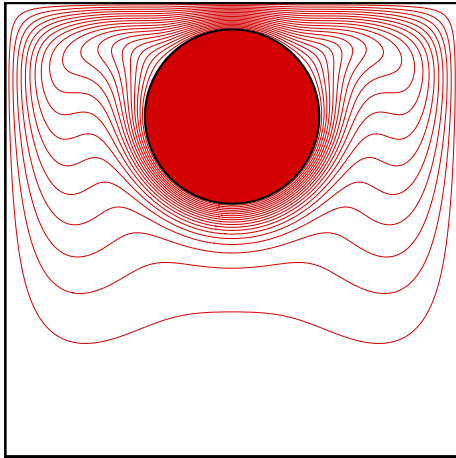


Fig. 18. Predicted isotherms at $\phi = 180^\circ$, $Ra = 3 \times 10^5$, and $L/D = 2.6$.

the cavity wall (T_{cav}) and cylinder wall (T_{cyl}) maintained at different temperatures and driven by the buoyancy force. Fig. 8 shows

the geometric set up, where ϵ is the distance between the cavity and cylinder center, R is the cylinder radius, and ϕ is the angle between lines \overline{AB} and \overline{BC} . For laminar convection in this flow configuration, the viscous heat dissipation is assumed to be negligible. The temperature difference between the walls introduces a temperature gradient in the fluid, and the consequent density difference induces a convective fluid motion. The variations of the eccentric inner cylinder produce different flow patterns and hence heat transfer characteristics.

With the Boussinesq approximation, the buoyancy term is assumed to depend linearly on the temperature as,

$$\rho \vec{G} = \rho \beta \mathbf{g} (T - T_m) \vec{j} \quad (51)$$

where β is the thermal expansion coefficient, \mathbf{g} is the acceleration due to gravity, $T_m = (T_{cav} + T_{cyl})/2$ is the average temperature, and \vec{j} is the vertical direction opposite to that of gravity. To account for this Buoyancy induced force, an extra forcing term F_i is added to Eq. (1) and is expressed as [32]

$$F_i = 3\omega_i \frac{\vec{G} \cdot \vec{e}_i}{c} \quad (52)$$

Other forms of forcing term accounted for the discrete effect could also be adopted [33]. It is noted that the compressibility may influence the results, and this can be eliminated by incompressible model [34]. However, since the present Mach number is low, therefore this influence could be neglected [17].

The major control parameter is the Rayleigh number $Ra = \beta \mathbf{g} \Delta T L^3 Pr / \nu^2$ associated with the heat transfer within the fluid, where L is the height or width of the cavity, ΔT is the temperature difference between inner and outer walls. The Nusselt number is also an important dimensionless parameters in describing the convective heat transport. Velocity boundary conditions are applied to all boundaries for modeling the flow field, where the domain is covered by a lattice sizes of 150×150 , 200×200 , and 300×300 , respectively for 10^4 , 10^5 and 10^6 . The proposed Dirichlet thermal boundary conditions are applied at the cavity and cylinder walls.

Table 1 shows the predicted Nusselt number distributions of the concentric cylinder setup at different Rayleigh numbers and cavity length and cylinder diameter ratios (L/D). The local and surface-averaged Nusselt numbers are defined as

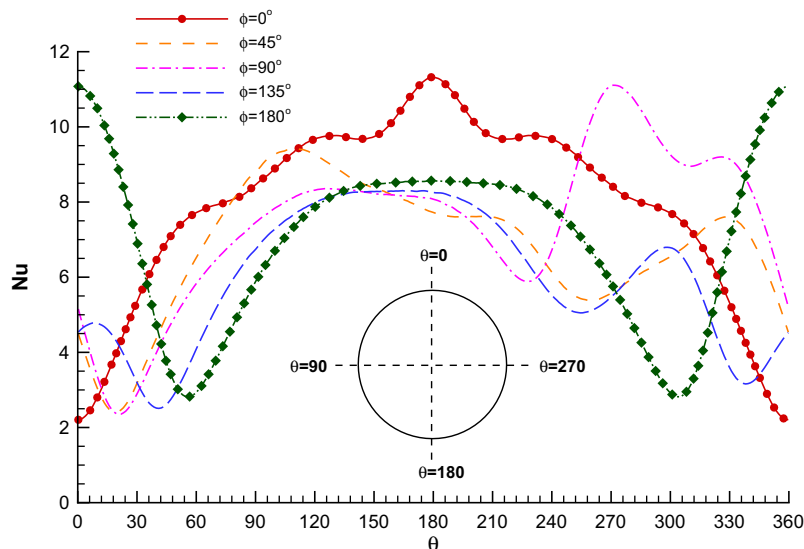


Fig. 19. Comparison of local Nusselt number distribution along the surface of the inner cylinder at different ϕ for $Ra = 3 \times 10^5$, and $L/D = 2.6$.

$$h = -k \frac{\partial T}{\partial n} \bigg|_{\text{wall}}, \quad \text{and} \quad Nu = \frac{hS}{k}, \quad (53)$$

$$\bar{h} = \frac{1}{2\pi} \int_0^{2\pi} h \, d\theta, \quad \text{and} \quad \bar{Nu} = \frac{\bar{h}S}{k}. \quad (54)$$

where n is the normal direction along the boundary and the characteristic length S is defined the same as in [2], i.e. half of the perimeter of the circular cylinder. The predicted surface-averaged Nusselt number (\bar{Nu}) is observed to increase in tandem with the L/D ratio, and this is consistent with the findings of Moukalled and Acharya [2] and Shu et al. [35]. The present results are also compatible with the two results, indicating the capability of the present technique. Table 2 also shows the predicted \bar{Nu} and Figs. 9–18 show the predicted streamlines and isotherms of the eccentric cylinder setup ($\epsilon = 0.25 L$) but at different location angles ($\phi = 0^\circ$ – 180°) when $Ra = 3 \times 10^5$. It can be observed that the eccentricity does influence the thermal field, and hence the streamlines. It is clear that beyond $\phi > 135^\circ$, the upward thermal plume is suppressed as the cylinder approaches the top wall, which is also reflected from the streamline distributions.

Fig. 19 further shows the distributions of local Nusselt numbers along the surface of the elliptic cylinder at different ϕ . When $\phi = 0^\circ$, symmetric Nu distributions with respect to vertical central line can be observed, where locally minimum and maximum Nu locate at upper and lower parts of the circular surface, respectively. It is clear that the local minimum of cylinder wall Nusselt number migrates from $\theta = 0$ to 55 and 305, while the maximum migrates from $\theta = 180$ to 0 in tandem with the increase of ϕ . The eccentricity does influence the distributions of Nusselt numbers.

5. Conclusion

In this paper, the previously proposed technique [24] to model complex geometry flows is extended to model the thermal flow with stationary embedded complex solid object. Present thermal LBM simulation is applied throughout the computational domain even within the solid object. Therefore, two different boundary conditions are addressed. The boundary condition along the flat computational domain, where the boundary coincides with the lattice, is similar to that proposed by Ho et al. [27] and Liu et al. [18] for the hydrodynamic and thermal boundary conditions, respectively. Here, the curved boundary as in [24] is represented by a series of Lagrangian markers. The temperature of node adjacent to the solid boundary is obtained by linear interpolation between the Lagrangian marker and the second fluid node further away. Then distribution functions originates from the solid domain at the nodes adjacent to the solid curved boundary are modified using known distribution functions and correctors, where the correctors at these nodes are obtained directly from the definition of temperature. The technique is examined by simulating thermal Couette flow with wall injection, transient thermal flow induced by an abruptly rotating heated ring and natural convection in an annulus between a square outer cavity and a circular inner cylinder. Numerical simulations indicate that this method is second order accurate, and all the numerical results are compatible with the benchmark solutions.

It should be noted that a challenge of the Cartesian-grid-based method is to compute time evolving moving boundary problems. In particular, a point in the solid can become a point in the fluid (or, vice versa) at the next time step. It produces severe oscillations of the predicted lift and drag coefficients and also the Nusselt number [4]. This was alleviated by adopting a solid-body forcing strategy within the solid domain, wherein the velocity of the point within the solid is forced to equal the velocity of the moving object [4,29]. This technique should be further explored to pursue its suitability within the lattice Boltzmann framework.

Acknowledgments

The authors gratefully acknowledge the support by the National Science Council of Taiwan and Low carbon energy research center of National Tsing Hua University, and the computational facilities provided by the Taiwan National Center for High-Performance Computing.

References

- [1] Kuehn TH, Goldstein RJ. An experimental and theoretical study of natural convection in the annulus between horizontal concentric cylinders. *J Fluid Mech* 1976;74:695.
- [2] Moukalled F, Acharya S. Natural convection in the annulus between concentric horizontal circular and square cylinders. *J Thermophys Heat Transf* 1996;10:524.
- [3] Kim BS, Lee DS, Ha MY, Yoon HS. A numerical study of natural convection in a square enclosure with a circular cylinder at different vertical location. *Int J Heat Mass Transf* 2008;51:1888.
- [4] Liao CC, Lin CA. Simulations of natural and forced convection flows with moving embedded object using immersed boundary method. *Comput Methods Appl Mech Eng* 2012;213–216:58.
- [5] Liao CC, Lin CA. Influences of a confined elliptic cylinder at different aspect ratios and inclinations on the laminar natural and mixed convection flows. *Int J Heat Mass Transf* 2012. <<http://dx.doi.org/10.1016/j.jheatmasstransfer.2012.06.073>>
- [6] Qian YH, D'Humières D, Lallemand P. Lattice BGK model for Navier–Stokes equation. *Europhys Lett* 1992;17:479.
- [7] Chen S, Doolen GD. Lattice Boltzmann method for fluid flows. *Ann Rev Fluid Mech* 1998;30:329.
- [8] Yu DZ, Mei RW, Luo LS, Shyy W. Viscous flow computations with the method of lattice Boltzmann equation. *Prog Aesop Sci* 2003;39:329.
- [9] Yasuda T, Satofuka N. An improved entropic lattice Boltzmann model for parallel computation. *Comput Fluids* 2011;45:187.
- [10] Lin LS, Chen YC, Lin CA. Multi relaxation time lattice Boltzmann simulations of deep lid driven cavity flows at different aspect ratios. *Comput Fluids* 2011;45:233.
- [11] Shih CH, Wu CL, Chang LC, Lin CA. Lattice Boltzmann simulations of incompressible liquid–gas systems on partial wetting surfaces. *Philos Trans Roy Soc A – Math Phys Eng Sci* 2011;369:2510.
- [12] Falcucci G, Ubertini S, Biscarini C, Di Francesco S, Chiappini D, Palpacelli S, et al. Lattice Boltzmann methods for multiphase flow simulations across scales. *Commun Comput Phys* 2011;9:269.
- [13] Murayama T, Yoshino M, Hirata T. Three-dimensional lattice Boltzmann simulation of two-phase flow containing a deformable body with a viscoelastic membrane. *Commun Comput Phys* 2011;9:1397.
- [14] Bepalko D, Pollard A, Uddin M. Analysis of the pressure fluctuations from an LBM simulation of turbulent channel flow. *Comput Fluids* 2012;54:143.
- [15] McNamara G, Garcia AL, Alder BJ. Stabilization of thermal lattice Boltzmann models. *J Stat Phys* 1995;81:395.
- [16] He X, Chen S, Doolen GD. A novel thermal model for the lattice Boltzmann method in incompressible limit. *J Comput Phys* 1998;146:282.
- [17] Peng Y, Shu C, Chew YT. Simplified thermal lattice Boltzmann model for incompressible thermal flows. *Phys Rev E* 2003;68:026701.
- [18] Liu CH, Lin KH, Mai HC, Lin CA. Thermal boundary conditions for thermal lattice Boltzmann simulations. *Comput Math Appl* 2010;59:2178.
- [19] Lallemand P, Luo LS. Hybrid finite-difference thermal lattice Boltzmann equation. *Int J Mod Phys B* 2003;17:41.
- [20] Lallemand P, Luo LS. Theory of the lattice Boltzmann method: acoustic and thermal properties in two and three dimensions. *Phys Rev E* 2003;68:036706.
- [21] Filippova O, Hänel D. Grid refinement for lattice-BGK models. *J Comput Phys* 1998;147:219.
- [22] Mei R, Luo LS, Shyy W. An accurate curved boundary treatment in the lattice Boltzmann method. *J Comput Phys* 1999;155:307.
- [23] Lallemand P, Luo LS. Lattice Boltzmann method for moving boundaries. *J Comput Phys* 2003;184:406.
- [24] Chang C, Liu CH, Lin CA. Boundary conditions for lattice Boltzmann simulations with complex geometry flows. *Comput Math Appl* 2009;58:940.
- [25] Zou Q, He X. On pressure and velocity boundary conditions for the lattice Boltzmann BGK model. *Phys Fluids* 1997;9:1591.
- [26] Junk M, Yang ZX. One-point boundary condition for the lattice Boltzmann method. *Phys Rev E* 2005;72:066701.
- [27] Ho CF, Chang C, Lin KH, Lin CA. Consistent boundary conditions for 2D and 3D laminar lattice Boltzmann simulations. *CMES – Comp Model Eng Sci* 2009;44:137.
- [28] Hecht M, Harting J. Implementation of on-site velocity boundary conditions for D3Q19 lattice Boltzmann simulations. *J Stat Mech – Theory Exp* 2010:P01018.
- [29] Liao CC, Chang YW, Lin CA, McDonough JM. Simulating flows with moving rigid boundary using immersed-boundary method. *Comput Fluids* 2010;39:152.
- [30] Chen DJ, Lin KH, Lin CA. Immersed boundary method based lattice Boltzmann method to simulate 2D and 3D complex geometry flows. *Int J Mod Phys* 2007;18:585.

- [31] Mai HC, Lin KH, Yang CH, Lin CA. A thermal lattice Boltzmann model for flows with viscous heat dissipation. CMES – Comp Model Eng Sci 2010;61:45.
- [32] He X, Zou Q, Luo LS, Dembo D. Analytic solution of simple flows and analysis of nonslip boundary conditions for the lattice Boltzmann BGK model. J Stat Phys 1997;87:115.
- [33] Guo ZL, Zheng CG, Shi BC. Discrete lattice effects on the forcing term in the lattice Boltzmann method. Phys Rev E 2002;65:046308.
- [34] He X, Luo LS. Lattice Boltzmann model for the incompressible Navier–Stokes equation. J Stat Phys 1997;88:927.
- [35] Shu C, Xue H, Zhu YD. Numerical study of natural convection in an eccentric annulus between a square outer cylinder and a circular inner cylinder using DQ method. Int J Heat Mass Transf 2001;44:3321.